SUPPLEMENTAL INFORMATION

Additional Model Discussion

Equation 4 can be used to obtain an expression for the resistance degradation rate, $\frac{1}{R_{P,C}}\left(\frac{dR_{P,C}}{dt}\right)$. The thick electrode limit in eq. 4 is used since it provides the best performance (lowest $R_{P,C}$) for any given cathode material, and is readily reached for typical electrode thicknesses of ~ 20 μm (see Figure S9). Taking the time derivative of $R_{P,C}$ yields

$$\frac{1}{R_{P,C}}\left(\frac{dR_{P,C}}{dt}\right) = \frac{1}{8\left(t + {l_{c,0}}^4/K_D\right)} \qquad (1s)$$

This illustrates that the degradation rate increases with the rate of cation diffusion K_D, and increases with decreasing initial infiltrate particle size $l_{c,0}$, as seen for example in Figure 4. A more practical expression can be developed by noting that one typically requires a target cathode resistance $R_{P,C}^T$ to achieve desired cell power density. Using the value $R_{P,C}^T$, with *t* = 0 for simplicity, and again using eq. 4 in the thick-electrode limit, yields

$$R_{P,C}^T = \sqrt{\frac{R_S l_{c,0}}{\sigma_{ion} C f}} \qquad (2s)$$

Solving eq. 2s for $l_{c,0}$ and substituting into eq. 1s with *t* = 0 yields the initial degradation rate for an initial particle size that yields the desired $R_{P,C}^T$:

$$\frac{1}{R_{P,C}}\left(\frac{dR_{P,C}}{dt}\right)_{t=0} = \frac{K_D R_S^4}{8\,(R_{P,C}^T)^8 \sigma_{ion}^4 C^4 f^4} \qquad (3s)$$

This shows that minimizing the MIEC surface resistance and maximizing the conductivity of the ionically-conducting phase are very important for minimizing degradation rate, but that cation diffusion kinetics also play an important role. Note that the initial degradation rate is a good approximation of the long-term degradation in cases where degradation rate is relatively low (see, for example, Fig. 3); these are, of course, the cases that are of actual practical interest. Based on eq. 3s, a figure of merit for an intermediate-temperature cathode materials set to achieve both low polarization resistance and low degradation rate is $K_DR_S^4/\sigma_{ion}^4$. For the present case of composite cathodes, K_D and R_S refer to the MIEC phase and σ_{ion} refers to the ionic conductor phase. For the case of a single-phase MIEC cathode, the MIEC plays both roles such that σ_{ion} is a property of the MIEC.

Since the aim of cathode development is typically to minimize cell operating temperature, it is instructive to introduce the temperature dependences of the transport properties, *i.e.,* $K_D = K_{D,0}exp(-E_D/kT)$, $R_S = R_{S,0}exp(E_S/kT)$, and $\sigma_{ion} = \sigma_{i,0}exp(-E_i/kT)$, where E_D is the activation energy for cation diffusion, E_S is the activation energy of the MIEC surface resistance,[36], and E_i is the activation energy of the oxygen ion conductivity. Substituting these into eq. 3s and gathering the temperature-dependent terms yields

$$\frac{1}{R_{P,C}}\left(\frac{dR_{P,C}}{dt}\right)_{t=0} = \frac{K_{D,0}R_{S,0}^{4}}{8\,(R_{P,C}^{T})^{8}\sigma_0^4C^4f^4}e^{(4E_S+4E_i-E_D)/kT} \qquad (4s)$$

The argument in the exponential term in eq. 4s should be positive in all cases. In the case of SSC, for example, E_S ~ 1.5 eV,[36], E_i ~ 0.6 eV for GDC,[37], and E_D = 2.81 eV from the present results. Thus, the overall activation energy in the exponential term is ~ 5 eV, such that eq. 4s predicts a rapid increase in degradation rate with decreasing temperature. Although this result may seem counter-intuitive at first glance, it is reasonable considering that it arises from the constraint of maintaining a target cathode resistance - this requires much smaller cathode feature sizes as temperature decreases. Note that eq. 4s gives the initial slopes of the degradation rates shown in Figure S7. Comparison of Figures S7 (a) and (b) shows the strong increase in degradation rate with decreasing target cathode resistance $R_{P,C}^{T}$; as indicated in eq. 2s, a factor of 2 decrease in $R_{P,C}^{T}$ necessitates a four-fold decrease in initial feature size, exacerbating coarsening. Finally, the key conclusion based on eq. 4s is that the activation energies for cation diffusion, in addition to those for oxygen transport, are important criteria in achieving an intermediate-temperature cathode that provides both low polarization resistance and low degradation rate.

Supplemental Tables

Table S1. Average SSC particle sizes estimated from SEM images of as-prepared electrodes and electrodes coarsened at 800 °C

Temperature 800 °C	
Time	**Size**
0	50 nm
400	65 nm
1500	173 nm

Table S2. Cathode microstructural parameters obtained from 3D tomographic reconstructions, as shown in the representative images in Figure S1.

Sample	GDC Scaffold As Fired	SSC-GDC Annealed
Porosity (%)	53.88	33.44
Particle Surface Area per Electrode	7.56	8.85

Volume (um^{-1})		
Particle Specific Surface Area (um^{-1})	16.39	13.30

Table S3. Model Parameters determined by fitting degradation data for SSC and LSCF cathodes

Sample	SSC	LSCF
E_d (eV)	2.81	2.90
$K_{D,0}$ (cm^2/s)	1.85x10^{-13}	8.98x10^{-13}
R^s at 600 °C (Ω·cm^2)	25	28.5
L (cm)	0.002	0.002
σ (S/cm)	0.0024	0.003
C	5-7	6
f	0.2-0.25	0.12
$l_{c,0}$ (cm)	5.0x10^{-5}	3.8x10^{-5}

Supplemental Figures

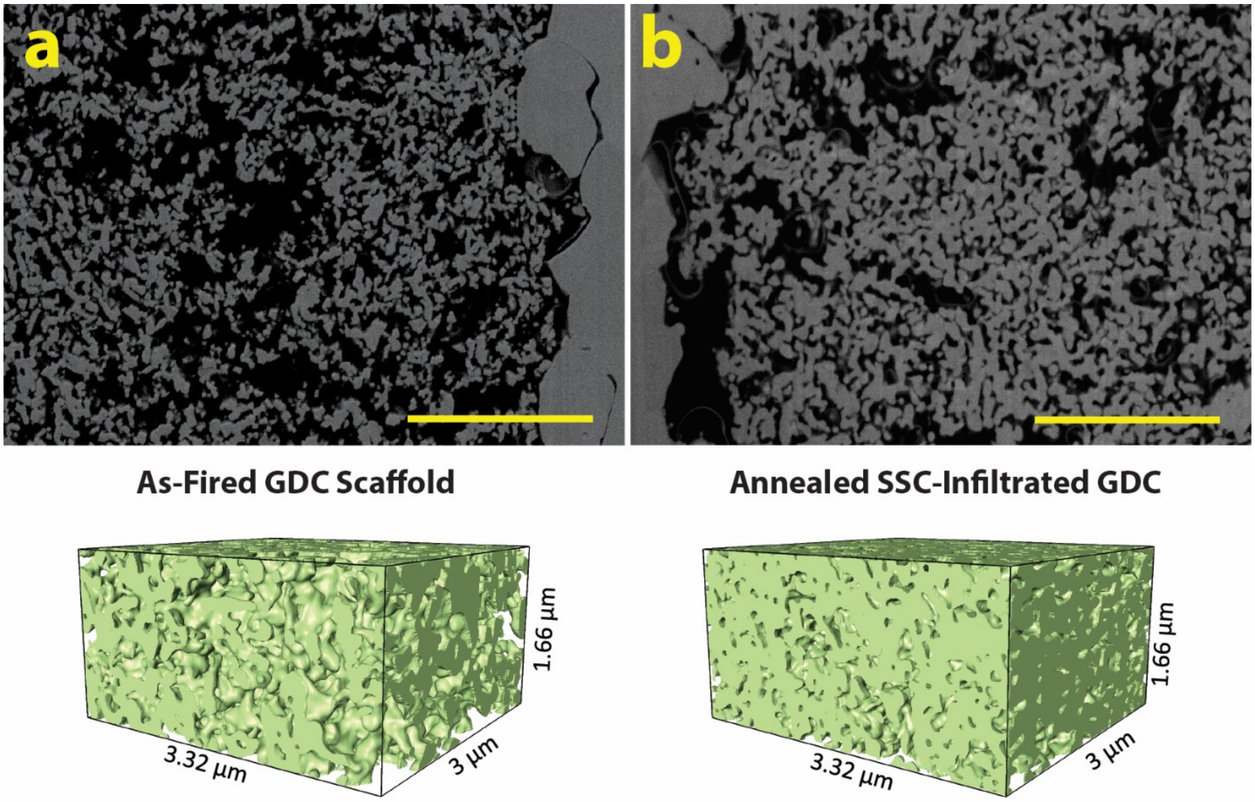

Figure S1. Cross-sectional SEM images and FIB-SEM 3D reconstructions of GDC scaffold (A) and GDC scaffold infiltrated with SSC (B). The GDC electrolyte is on the right side in A, and the left side in B. Samples were prepared for imaging by FIB polishing and epoxy infiltration. The solid fraction is displayed in green while the pore fraction is transparent. Note that the 3D views show smaller regions cropped from the full reconstruction volumes, for clarity. Scale bars are 3 microns.

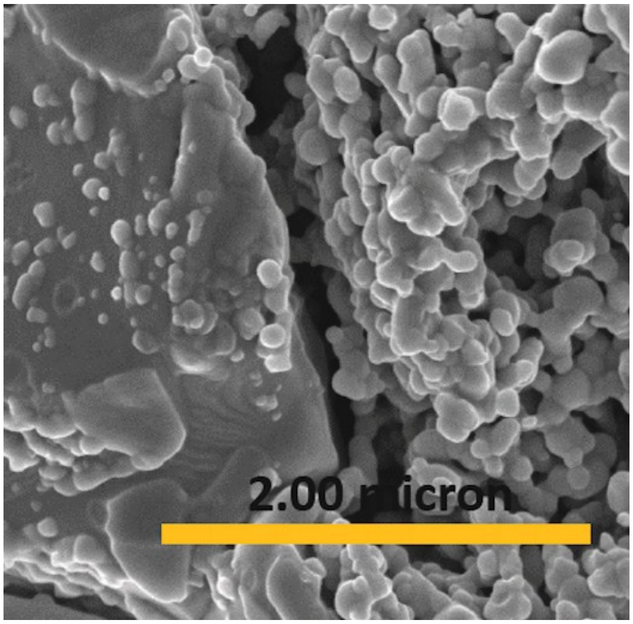

Figure S2. SEM fracture cross sectional image of an SSC-infiltrated GDC electrode. The left side shows a portion of the electrolyte, while the right side shows the cathode. Although the infiltrated SSC particles are clearly seen on a flat portion of the GDC electrolyte, they are difficult to resolve within the porous electrode.

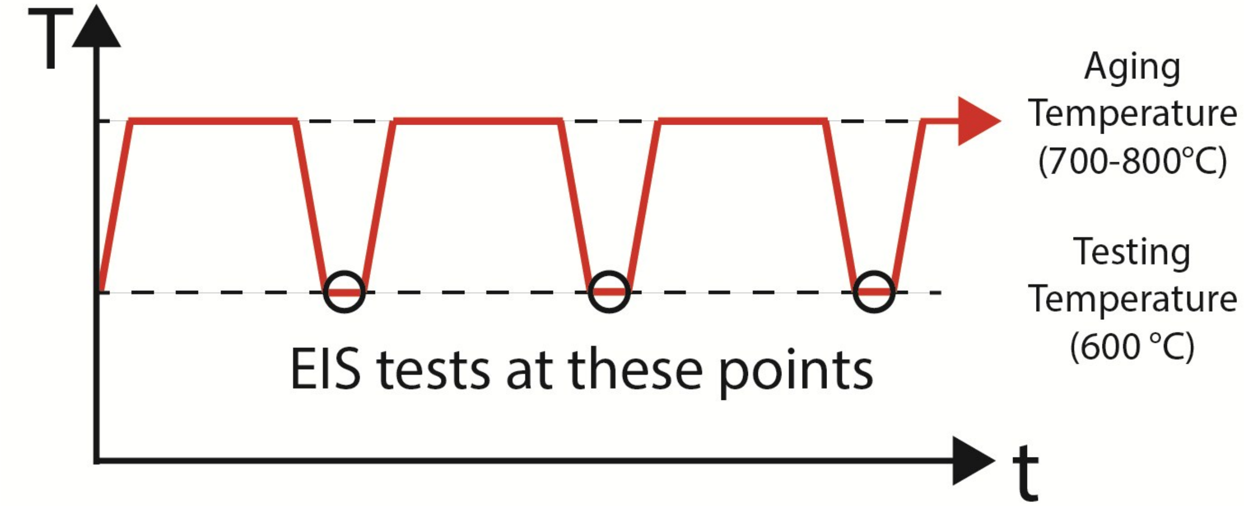

Figure S3. Illustration of the testing program used to collect EIS data during coarsening. The testing interruptions constituted ~4% of the total testing time, such that the cells were at the ageing temperature for ~ 96% of the testing time.

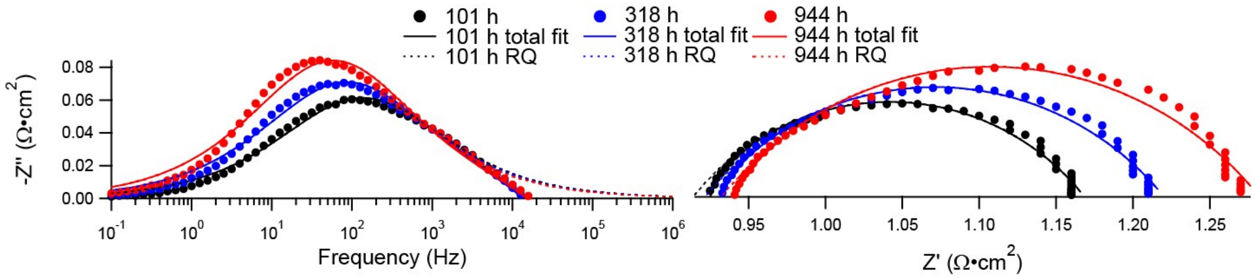

Figure S4. Bode and Nyquist plots of EIS data taken at different times during a life test of an SSC-GDC electrode aged at 800 °C and measured EIS tested at 600 °C in air. There appears to be one dominant response, initially centered at ~ 100 Hz. The results illustrate the steady increase in cathode polarization resistance with increasing time, along with a slight shift to lower frequency. The shape of the cathode response did not change appreciably during the life tests. The cathode polarization resistance values shown in Figures 2 and S7 were obtained as the difference between the real-axis intercepts in the Nyquist plots. Circuit model fits are also shown from an L-R-RQ equivalent circuit showing both the total fit and the RQ element. The difference between the high frequency intercept and the calculated RQ intercept is on the order of 1% difference.

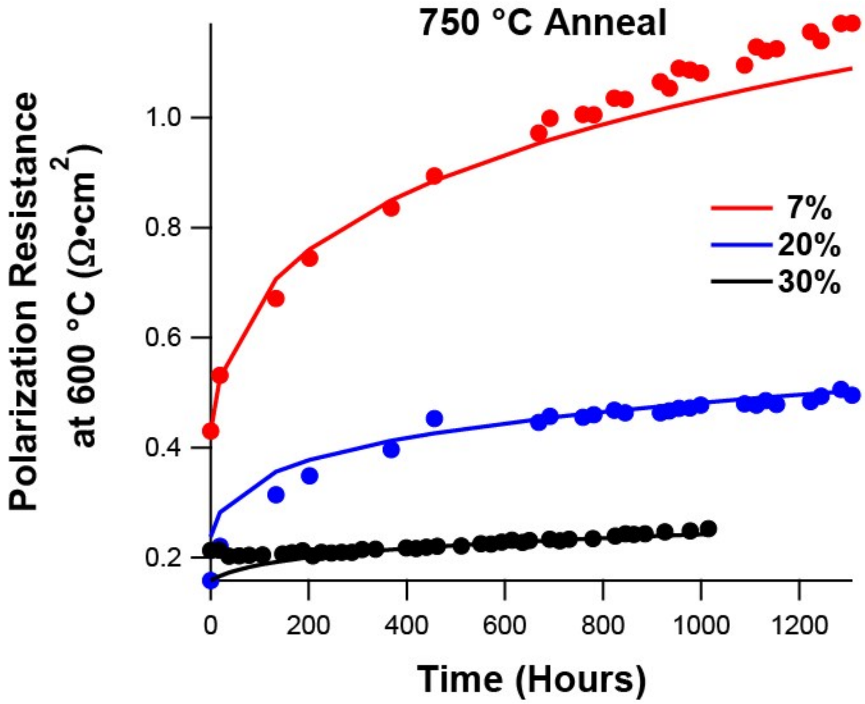

Figure S5. Cathode polarization resistance of SSC-infiltrated symmetric cells with different SSC volume fractions *f*, taken from EIS data measured in air at 600 °C (see Figure S4), versus ageing time at 750 °C. Also shown are the overall best fits to the data using eq. 4 with the $K_{D,0}$ and E_D values given in Table S3; other parameters were slightly different from those used in Figure 2, presumably because these measurements were made on a different batch of cells. For the *f* = 30% cathode, a larger initial feature size $l_{c,0}$ - 70 nm instead of 50 nm – was used accounting for a tendency for infiltrated particles to overlap at high SSC loading, leading to larger effective feature sizes.

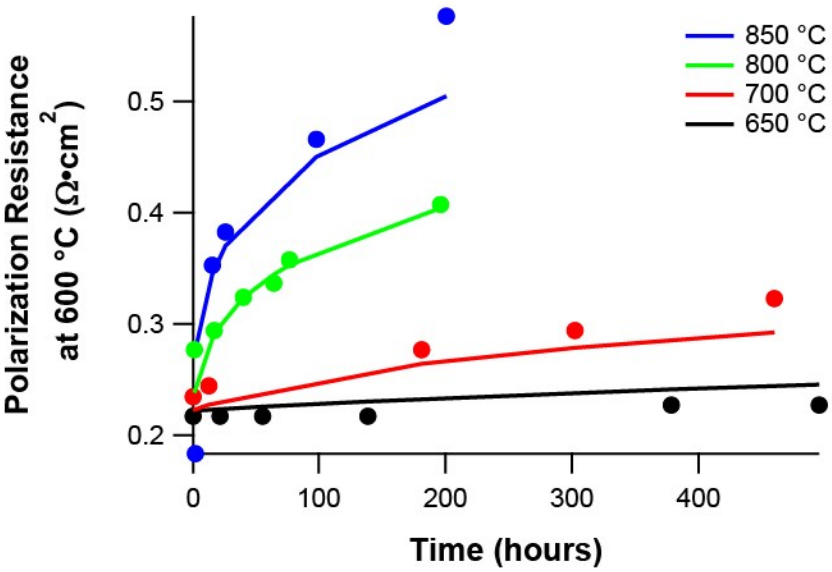

Figure S6. Cathode polarization resistance of LSCF-infiltrated symmetric cells aged at temperatures ranging from 650-850 °C taken from EIS data measured in air at 600 ^{o}C (see Figure S3), (from Ref [15]). Also shown are the overall best fits to the data using eq. 4 with the $K_{D,0}$ and E_D values given in Table S3.

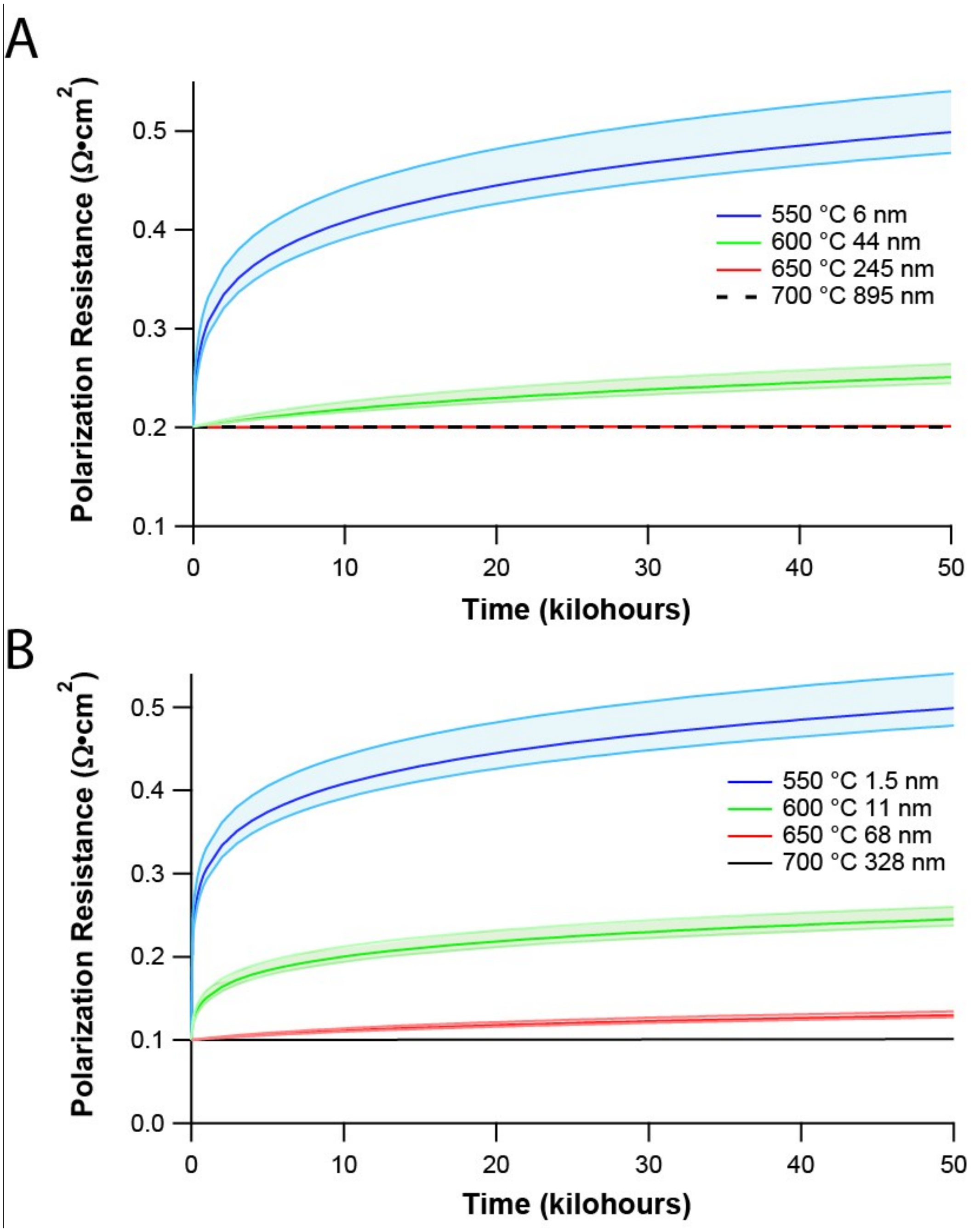

Figure S7. Predicted polarization resistance versus time for infiltrated SSC-GDC cathodes designed to yield; the initial cathode SSC feature size was chosen for each operating temperature in order to achieve an initial $R_{P,C}$ of (a) 0.2 Ω·cm^2 or (b) 0.1 Ω·cm^2. This illustrates that the decrease in operating temperature that can be realized via reduction of cathode MIEC particle size is ultimately limited by excessive coarsening. Solid curves indicate predictions using best fit values, while the broader shading indicates predictions for the range of $K_{D,0}$ and E_D values that provide reasonable fits, as described in Figure 2.

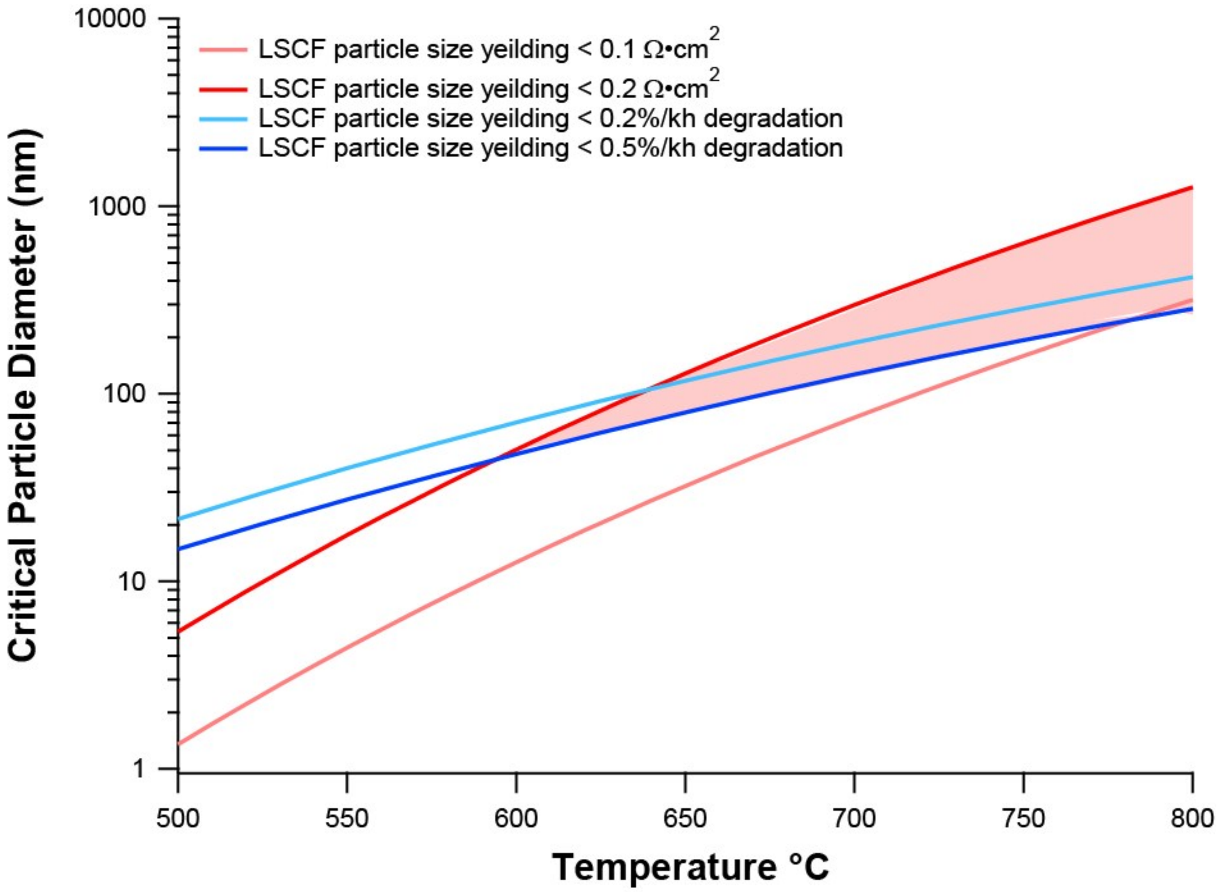

Figure S8 A plot of critical LSCF particle diameters that provide target performance and stability values, versus cell operating temperature The red curves show the diameter yielding target cathode resistance values of $R_{P,C}^{T}$ = 0.2 or 0.1 Ω·cm^2. The blue curves show the diameter yielding target degradation rate ($\frac{1}{R_{P,C}}\left(\frac{dR_{P,C}}{dt}\right)$ = 0.5 or 0.2 %/kh). The shaded area shows the LSCF particle sizes and cell operating temperatures that yield the desired stability and performance; for clarity, the shading is shown only for the target values $R_{P,C}^{T} \leq$ 0.2 Ω·cm^2 and ($\frac{1}{R_{P,C}}\left(\frac{dR_{P,C}}{dt}\right)$ ≤ 0.5 %/kh. Note that coarsening data for infiltrated LSCF is sparser than for SSC, so these predictions have greater uncertainty than those shown in Figure 4.

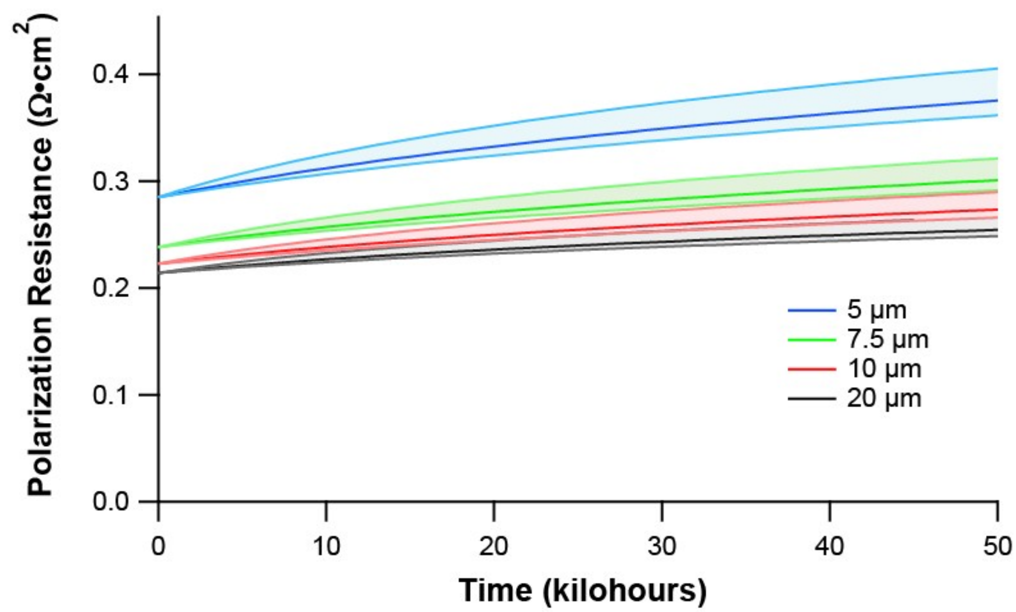

Figure S9. Predicted resistance versus time for infiltrated SSC-GDC cathodes operated at a temperature of 600 °C, for a SSC particle size of 50 nm and electrode thicknesses of 5, 7.5, 10, and 20 μm. Note that the resistance does not decrease measurably further when the thickness is increased above 20 μm. This illustrates that thickness has relatively little effect on long-term stability, and that most of the electrochemical processes occur in a cathode region within 10 μm of the electrolyte.